remote sensing

MDPI

Article

Seasonal Variation in the Mesospheric Ca Layer and Ca^+ Layer Simultaneously Observed over Beijing (40.41°N, 116.01°E)

Yuchang Xun [1,2], Peng Zhao [1,2], Zelong Wang [2,3], Lifang Du [2], Jing Jiao [2], Zhishan Chen [1,2], Haoran Zheng [2], Shaohua Gong [4] and Guotao Yang [2,*]

1 College of Physics, College of Electronic Information and Optical Engineering, Taiyuan University of Technology, Taiyuan 030024, China; xunyuchang@tyut.edu.cn (Y.X.); zhaopeng1282@link.tyut.edu.cn (P.Z.); chenzhishan1477@link.tyut.edu.cn (Z.C.)
2 State Key Laboratory of Space Weather, National Space Science Center, Chinese Academy of Sciences, Beijing 100190, China; zlwang@just.edu.cn (Z.W.); lfdu@nssc.ac.cn (L.D.); jjiao@swl.ac.cn (J.J.); hrzheng@spaceweather.ac.cn (H.Z.)
3 School of Science, Jiangsu University of Science and Technology, Zhenjiang 212100, China
4 School of Physics and Electronics Engineering, Hainan Normal University, Haikou 571158, China; shhgong@hainnu.edu.cn
* Correspondence: gtyang@swl.ac.cn

Abstract: In March 2020, an all-solid-state dual-wavelength narrow-band lidar system was deployed. A total of 226 nights spanning from March 2020 to July 2022 were employed in order to investigate the seasonal variations of calcium atoms and ions in the mesosphere over Beijing (40.41°N, 116.01°E). The Ca^+ layer shows general annual variation, while a semiannual variation is observed on the Ca layer. The calcium atomic column densities ranged from 2.0×10^6 to 1.1×10^8 cm^{-2}, and the calcium ion column densities ranged from 1.6×10^6 to 4.2×10^8 cm^{-2}. The mean centroid heights of Ca^+ and Ca are 98.6 km and 93.0 km, respectively, and the centroid heights of Ca^+ and Ca are mostly influenced by annual variations. The seasonal variation in the Ca^+ and Ca layers in Beijing exhibits similarities to that of Kühlungsborn (54°N). While the peak density of Ca^+ in Beijing are similar to those observed in Kühlungsborn, the peak density of the Ca layer in Beijing is about half of that reported in the Ca layer at 54°N. We provide an explanation for the disparities in the column abundance and centroid altitude of the Ca layer between Yanqing and Kühlungsborn, discussing variations in neutralization among different metal ions.

Keywords: lidar; OPO; OPA; seasonal variation; Ca layer; Ca^+ layer

check for updates

Citation: Xun, Y.; Zhao, P.; Wang, Z.; Du, L.; Jiao, J.; Chen, Z.; Zheng, H.; Gong, S.; Yang, G. Seasonal Variation in the Mesospheric Ca Layer and Ca^+ Layer Simultaneously Observed over Beijing (40.41°N, 116.01°E). *Remote Sens.* **2024**, *16*, 596. https://doi.org/10.3390/rs16030596

Academic Editor: Michael Obland

Received: 10 November 2023
Revised: 18 January 2024
Accepted: 31 January 2024
Published: 5 February 2024

1. Introduction

Metallic atoms and ions are found in the mesosphere and lower thermosphere (MLT) at altitudes ranging from approximately 75 to 110 km. Recently, an observation found that the Na atom and Ca ion extended up to 200 and 300 km, respectively [1,2]. These metal particles are released into the atmosphere by processes such as ablation and sputtering, which occur when cosmic dust interacts with the Earth's atmosphere [3]. Since the year 1929, when Slipher initially observed the presence of sodium fluorescence lines in the twilight airglow [4], various ground-based instruments such as airglow and lidar have been employed for several decades to study the behavior of metal atoms, including sodium, iron, potassium, nickel, and calcium. The sodium atom was the first to be detected and is currently the most extensively studied atom due to its comparatively high density, significant backscattering cross-section, and the convenient acquisition of sodium atomic resonance absorption lines that match to lasers technology. Ca^+ is the only metallic ion species that can be detected by ground-based equipment since other ions that need short UV wavelengths to excite are out of reach from the ground because of atmosphere absorption [5].

The initial lidar measurements of the Ca and Ca^+ layers were conducted at Observatoire de Haute Provence, located at coordinates 44°N and 6°E, during the months of December 1982 and July 1983, respectively. The column density of calcium (Ca) atoms is around 1.5×10^7 cm^{-2}, while the column density of calcium ions (Ca^+) exceeds 6×10^7 cm^{-2} [6]. The following lidar observations at multitudes showed the column density of Ca to be between 2×10^6 cm^{-2} and 10.7×10^7 cm^{-2} and the column density of Ca^+ to be between 5×10^6 cm^{-2} and 8.65×10^8 cm^{-2} at Observatoire de Haute Provence (44°N, 6°E), Urbana (40°N, 88°W), and island Rügen (55°N, 13°E), respectively [5–8], but these observations were primarily made in the summer, the autumn, and December. All of these papers focused only on case studies. Gerding et al. [9] reported the current analysis of the annual variation in Ca and Ca^+ layers for the period from December 1996 to December 1998. The study includes 112 nights of Ca soundings and 58 nights of Ca^+ sounding. Plane et al. built a large database of neutral and ion–molecule reaction kinetics of Ca species, measured over the past decade, and incorporated it into the Whole Atmosphere Community Climate Model (WACCM). The model successfully simulates the height and width of the Ca layer, as well as the minimum in springtime and the broad maximum during the second half of the year [10].

Nevertheless, it is worth noting that the spatial distribution of metal atoms exhibits considerable variation in density across different latitudes and locations, which is distinct from the temporal variations observed in other metal compositions, as previously discussed. For example, the densities of sodium (Na) reach their peak levels during the winter season and their minimum levels during the summer season. The density increases as one moves towards higher latitudes. The column density measurements at three locations, namely, Hainan, China (19.99°N, 110.34°E), Wuhan, China (30.5°N, 114.4°E), and Amundsen-Scott South Pole Station (90°S), were reported as 1.51×10^9 cm^{-2}, 2.5×10^9 cm^{-2}, and 4.3×10^9 cm^{-2}, respectively [11–13]. In the region of middle and high latitudes, the density of Fe exhibits a peak during the winter season and a decline during the summer season. Conversely, in low latitudes, the densities of Fe reach their maximum during the spring season and experience a decrease during the fall season. The density exhibits similarity across low and high latitudes but demonstrates a decrease at mid-latitudes. The average column density of iron (Fe) at the Amundsen-Scott South Pole Station (located at 90°S) and the Arecibo Observatory (located at 18.35°N, 66.75°W) was measured to be 9.7×10^9 cm^{-2} and 9.73×10^9 cm^{-2}, respectively. However, in Wuhan, China (located at coordinates 30.5°N, 114.4°E), the average column density of iron (Fe) was measured to be 7.5×10^9 cm^{-2}, as reported in previous studies [12–14]. The K layer has similar densities at low and high latitudes. It has higher densities and large regional differences at mid-latitudes. The K layer densities show the maximum in winter and summer and the minimum in spring and autumn. The mean column density of K was 4.4×10^7 cm^{-2}, 4.61×10^7 cm^{-2}, and 8.41×10^7 cm^{-2} at the Kühlungsborn (54°N, 12°E), Arecibo, Puerto Rico (18.35°N, 66.75°W), and Beijing, China (40.41°N, 116.01°E) [15–17].

In comparison to the earlier dye lasers employed globally, the all-solid-state laser utilized in this study was developed in March 2020. For a long time, the technique has been employed to concurrently detect calcium atoms and calcium ions. Only seasonal variations in Ca and Ca^+ have previously been recorded for 54°N in the western hemisphere. In this study, we describe the seasonal variation in Ca and Ca^+ layers measured simultaneously from March 2020 to July 2022 at Yanqing station near Beijing (40.41°N, 116.01°E) to provide insight into the latitudinal and regional differences in the seasonal variations in Ca and Ca^+. Seasonal variations in Na, K, and Ni are also compared at the same station. Finally, this paper concludes with a brief discussion of the reasons for the seasonal variations in the Ca and Ca^+ layers. The simultaneous, common-volume lidar observations of seasonal variations in Ca and Ca^+ will further facilitate in-depth investigations into the chemical and dynamical processes between metal atoms and ions in the upper atmosphere.

2. Technique

2.1. The OPO Ca-Ca^+ Lidar

The all-solid-state dual-wavelength narrow-band lidar system is equipped to observe the Ca layer and the Ca^+ layer simultaneously. Compared with other metal atoms, the small density and weak signal were the main difficulties in the detection of Ca^+/Ca. Also, the energy and stability of dye lidar used in the past are relatively low. The dye lasers were replaced with two all-solid-state lasers from March 2020. The laser is based on optical parametric oscillation (OPO) and optical parametric amplification (OPA) technologies, which are primarily used to amplify signal light to produce a specific wavelength of laser [18,19].

The OPO lidar system comprises three main components: a transmitter system, a receiver system, and a data acquisition system. The laser transmitter system comprises several components, including a neodymium: yttrium/aluminum/garnet (Nd:YAG) laser, an optical parametric oscillator (OPO), an optical parametric amplifier (OPA), a frequency-doubling crystal, an optical lens, and a beam splitter. The pulsed Nd:YAG laser is utilized as the energy source to stimulate the operation of two optical parametric oscillators/optical parametric amplifiers (OPO/OPA). These devices are responsible for the production of laser beams at wavelengths of 786 nm and 846 nm. The OPO is utilized to generate laser pulses by oscillating the 786 nm and 846 nm lasers. Subsequently, a single-stage OPA is employed to amplify the laser's photon count. Furthermore, the seed laser produces a 532 nm laser beam by utilizing the second harmonic generation (SHG) module. This laser beam serves as a pump light source, supplying the necessary energy for the oscillation and amplification processes of the 786 nm and 846 nm lasers. The SHG module facilitates the generation of the 393 nm and 423 nm lasers from the 786 nm and 846 nm lasers, respectively [20].

The lasers with wavelengths of 393 nm and 423 nm were directed through beam-expanding mirrors in order to decrease the laser beam divergence angle and optimize its collimation. Subsequently, they were reflected by a total reflection mirror and subsequently directed into the Earth's atmosphere in a vertical orientation. The Cassegrain telescope, with a diameter of 1.23 m, is employed for the purpose of detecting resonance fluorescence photons emitted by the Ca and Ca^+ layers in the atmosphere. These optical signals are then relayed via optical fibers and subsequently transformed into electrical signals by photomultiplier tubes (PMTs).

The data acquisition system employs two data acquisition cards (MCS-PCI) to capture signals from the 423 nm channel and the 393 nm channel, correspondingly. The pulse counting method is employed to quantify the quantity of photons, with the signals being acquired and stored by an industrial computer. Table 1 presents the parameters of the Ca and Ca^+ lidar system.

Table 1. The Parameters of the Calcium Atoms and Calcium Ions Lidar.

Parameter	Ca	Ca^+
Laser wavelength (nm)	422.6728	393.3663
Laser linewidth (MHz)	169.3	154.6
Repetition rate (Hz)	15	15
Pulse energy (mJ)	31	30
Beam divergence (mrad)	0.5	0.5
Telescope aperture (m)	1.23	1.23
Focal length (m)	2.4	2.4
Fiber diameter (mm)	1.5	1.5
Optical filter FWHM (nm)	1	1
Time resolution (s)	66.7	66.7
Spatial resolution (m)	96	96
Count rate (MHz)	150	150

The lidar system utilizing optical parametric oscillator/optical parametric amplifier (OPO/OPA) technology exhibits notable attributes such as a high energy output (31 mJ and

30 mJ for Ca and Ca^+ ions, respectively), a narrow bandwidth (169.3 MHz and 154.6 MHz for Ca and Ca^+ ions, respectively), robust system stability, and the ability to generate a uniform and adjustable laser spot. The OPO lidar utilizes an all-solid-state technology, with the laser component providing control over the output spot. In contrast, dye lasers necessitate regular human interaction during the observation process and exhibit suboptimal uniformity in the output spot, which manifests as a crescent-shaped light spot [20]. The OPO lidar system exhibits notable stability and reliability, enabling sustained and consistent operation over extended durations. The OPO lidar also detected several noteworthy occurrences. For instance, on 15 July 2020, the Ca layer had a three-layer structure, whereas the Ca^+ layer displayed a two-layer structure. The presence of the Ca^+ layer was detected at an altitude below 90 km on 21 October 2020. From March 2020 to December 2021, there was a consistent monitoring of the Ca^+ layer within the E-F region. These special structures have not been observed before [2,20].

2.2. Data and Methods

In this paper, we use the simultaneous calcium atom and calcium ion lidar observation data from March 2020 to July 2022. Following the elimination of the noise caused by cloudy days, laser wavelength shifts, etc., the valid calcium atom data have 226 nights (1711 h in total), and the calcium ion data have 224 nights (1720 h in total). The recorded data on the same date in different years indicate that there were 82 nights with Ca and 78 nights with Ca^+. The process involves merging data from the same date but in separate years by multi-day averaging. This results in a total of 184 instances where observations of calcium atoms and calcium ions occur simultaneously. The raw data used for this analysis have a vertical resolution of 96 m and a time resolution of 33 s. Figures 1 and 2 present the statistical data pertaining to the observed hours and nights for Ca and Ca^+ lidar.

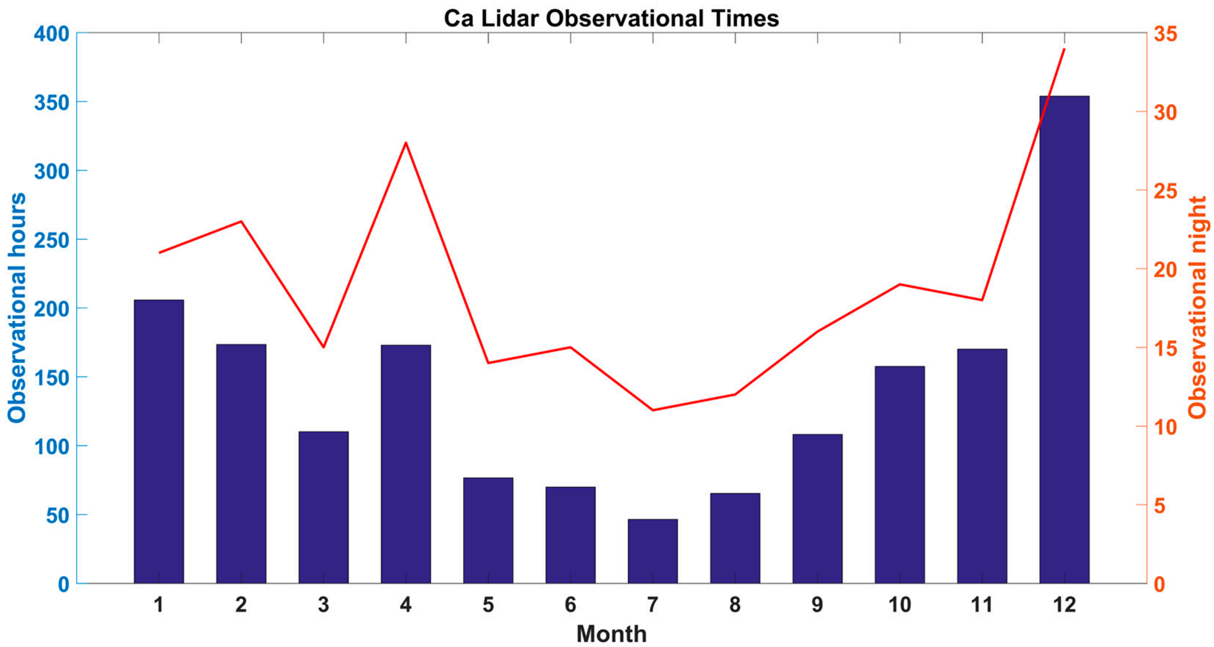

Figure 1. The observation time of Ca lidar (the number of nights and hours are represented by blue bars and red lines, respectively).

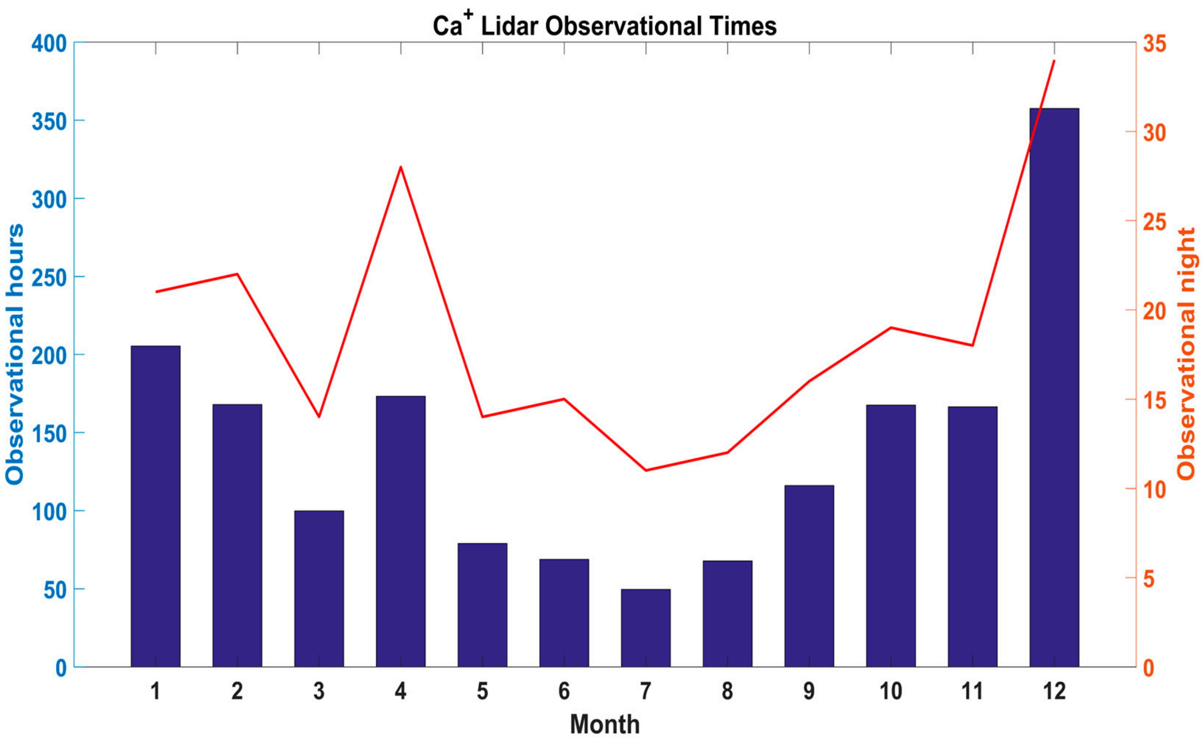

Figure 2. The observation time of Ca^+ lidar (the number of nights and hours are represented by blue bars and red lines, respectively).

The Ca or Ca^+ densities are calculated using the standard lidar equation:

$$n_M(z) = n_A(z_R)\left\{\frac{N_M(z) - N_B}{N_R(z_R) - N_B}\frac{z^2}{z_R^2} - \frac{n_A(z)}{n_A(z_R)}\right\}\frac{\sigma_R}{\sigma_M},\ M = \mathrm{Ca\ or\ Ca^+} \quad (1)$$

where M denotes Ca or Ca^+, $n_M(z)$ is M number density at altitude z; $n_A(z_R)$ is the atmosphere molecular number density at the reference altitude (z_R) taken from NRLMSISE-00; $n_A(z)$ is the atmosphere molecular number density at altitude z; $N_M(z)$ is the photon counts received at z; $N_R(z_R)$ is the photon counts received at z_R; σ_R is the Rayleigh backscattering cross-section; σ_M is the effective resonance fluorescence backscattering cross-section.

To improve the signal-to-noise ratio, we used Ca and Ca^+ data in this paper with a vertical resolution of 960 m and a time resolution of 330 s. To obtain the annual variation, the data were averaged for each night at the same altitude and fitted using least squares with the following equation [9,16,17,21]:

$$y = E + A_1 \cdot \cos\left(\frac{2\pi}{365}\cdot d - P1\right) + A_2 \cdot \cos\left(\frac{2\pi}{365/2}\cdot d - P2\right) \quad (2)$$

where y is the density value of Ca or Ca^+, E is the mean profile, A_1 is the amplitude of the annual oscillation, P1 is the initial phase of the annual oscillation, A_2 is the amplitude of the semiannual oscillation, P2 is the initial phase of the semiannual oscillation, and d denotes the day of the year at the data observation point.

At each height, a harmonic fit was applied to the data. The resulting fitted values were then compared to the observed values. The discrepancies between the fitted and observed values were further filtered using a Hanning window with a width of 91 days. Finally, the smoothed differences were added back to the fitted values [9,16,17,21]. The characteristic parameters, namely, the peak density, column density, centroid height, and RMS width, were computed based on the studies conducted by Gardner et al. [22] and Gong et al. [11].

3. Results

3.1. Seasonal Variation in the Ca and Ca^+ Layers

Figure 3a,b depict an example of nighttime variations in Ca and Ca^+ layers on 10 December 2020. The calcium atoms and calcium ions are distributed between 82 and 110 km. In Figure 3a, there is the first sporadic Ca layer (sporadic Ca layer references [23,24]): (1) At the same altitude, the peak density of sparse Ca layers is at least twice that of the background Ca layer. (2) The full-width-at-half-maximum (FWHM) of sparse Ca layers is less than 5.0 km, is distributed between 92.1 and 96.0 km, and persists from the initiation of observations until approximately 22:20 LT. The peak density, occurring around 21:00 LT, is approximately 153.1 cm^{-3}, and the corresponding altitude is approximately 94.1 km. The second sporadic Ca layer initiates around 22:00 LT, exhibiting a descending trend until approximately 4:20 LT, during which the altitude decreases from 102.7 km to 97.0 km. Subsequently, it undergoes a gradual ascent throughout the night, reaching an altitude of 97.9 km. The peak density is approximately 64.9 cm^{-3}, occurring at an altitude of approximately 100.8 km. Figure 3b illustrates three Ca^+ layers, with the nighttime variations in Ca^+ exhibiting more variability. The first sporadic Ca^+ layer corresponds to the Ca layer but has a longer duration, persisting from around 20:00 LT to approximately 02:20 LT. The altitude undergoes an initial descent from 102.7 to 94.1 km, followed by a brief ascent to 96.0 km, and ultimately descends to 93.1 km. The peak, occurring at approximately 20:21 LT, has a density of approximately 523.2 cm^{-3} at an altitude of around 94.1 km. The second sporadic Ca^+ layer appears at 21:16 LT, with an initial altitude of 99.8 km. It undergoes a brief ascent to approximately 103.7 km, almost concurrently with the ascent of the first Ca^+ layer, continuing until 22:40 LT. Subsequently, the Ca^+ layer exhibits a descending trend, reaching a final altitude of approximately 97.9 km. The peak of the second Ca^+ layer occurs around 01:30 LT, with a density of approximately 231.7 cm^{-3} at an altitude of around 97.9 km. The third sporadic Ca^+ layer emerges around 3:15 LT, displaying a descending trend and ultimately decreasing from 106.6 to 105.6 km.

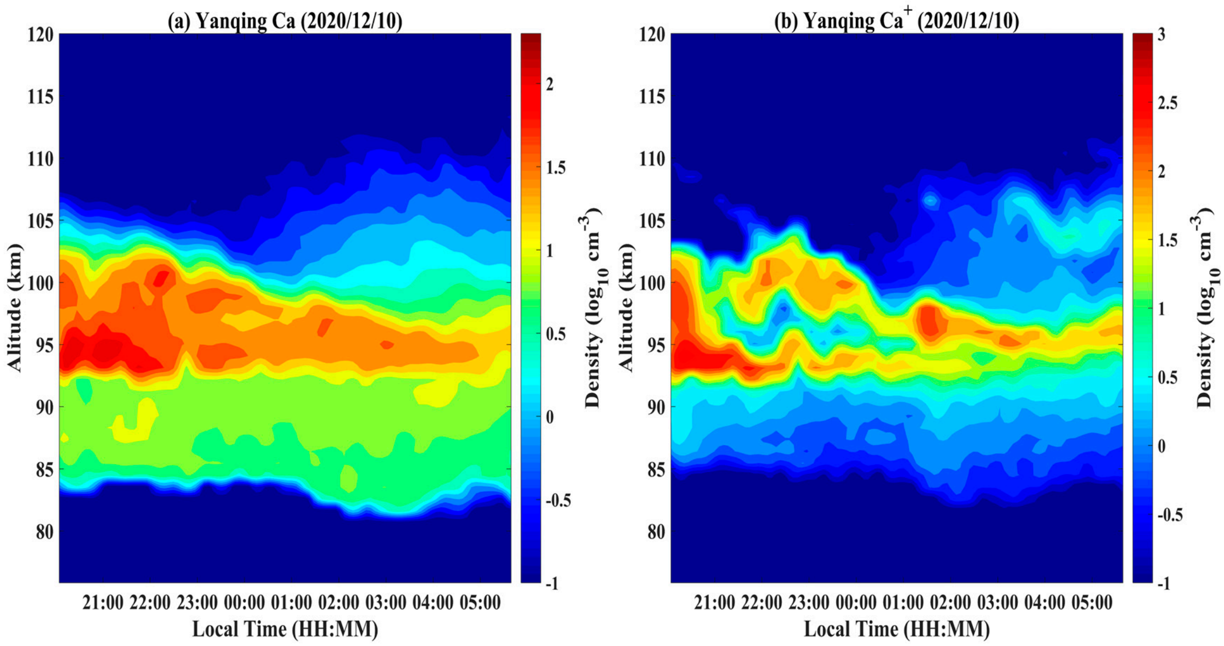

Figure 3. Contour of the nocturnal variation in the Ca and Ca^+ layers over Beijing: (**a**) Ca: 10 December 2020, (**b**) Ca^+: 10 December 2020.

Figure 4a,b show the seasonal variation in the density of Ca and Ca^+ layers, respectively.

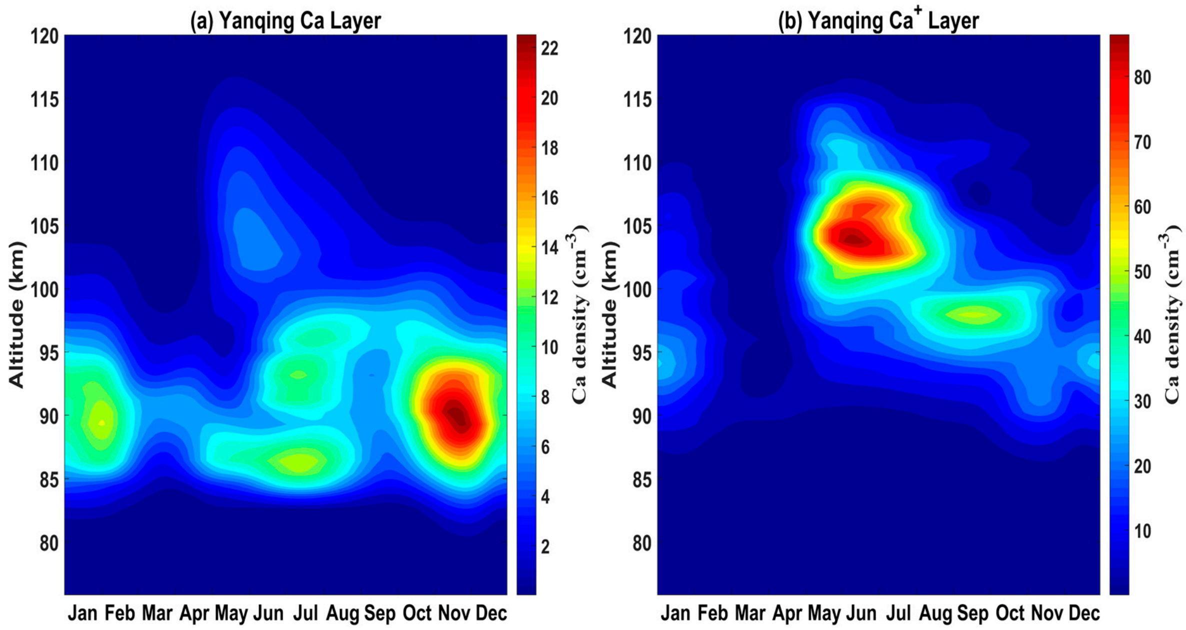

Figure 4. Contour of the annual variation in (**a**) Ca and (**b**) Ca^+ density over Beijing.

A semiannual variation in Ca densities can be observed, as depicted in Figure 4a. The maxima occur during the winter and summer seasons, with the winter maximum being larger than the summer maximum. The main layer is located within the altitude range of 80.6 to 103.7 km. In the month of November, the maximum density observed was 23.1 cm^{-3} at an altitude of 90.2 km. The other two peaks occur in winter (January/February) and summer (July), with a density of 13.6 cm^{-3} (peak at 89.3 km) and 13.4 cm^{-3} (peak at 86.4 km), respectively. The minimum density occurs in March. During the summer months of May to August, an upward extension of the main Ca layer takes place, resulting in the formation of a three-layer structure. The main layer lies between 82.6 and 100.8 km, with two sporadic layers: one between 85.0 and 90.0 km and the other between 90.0 and 100.0 km. The peak altitude within this layer is 93.1 km, with a corresponding density peak of 12.0 cm^{-3}. The thermosphere–ionosphere sporadic calcium layer (TISCa) is located above the main layer. The TISCa layer spans vertically from 100.0 to 116.0 km, with its highest density reaching approximately 6.1 cm^{-3} at an altitude of 103.7 km. The ratio of the summer peak density of the TISCa layer to the main layer is approximately 2.

It is worth mentioning that at an altitude of approximately 105 km, the frequency of Cas events is seen to be approximately 27% during the months of January to April, around 20% from October to December, and significantly higher at approximately 68% from May to September. During the summer season, there is a recurring phenomenon of occasional Ca layers at high altitudes that persist for numerous consecutive nights. In spring and winter, there are rare occurrences of high-altitude Ca layers that happen intermittently and have a shorter duration. This also suggests that it is easier to observe TISCa layers occurring above 100 km in summer.

Figure 4b displays the annual variation in the Ca^+ layer. The maximum density of the Ca^+ layer is observed during June. At an altitude of 103.7 km, the density reaches a value of 88.8 cm^{-3}. During the summer season, the layer consisting of Ca^+ has the greatest density throughout the altitude range of 100 to 115 km. Sporadic calcium ion (Ca^+s) layers exhibit a higher prevalence compared to Cas layers. Specific statistics for sporadic Ca and sporadic Ca^+ layers will be carried out in the next step. The Ca^+ layer has a secondary maximum in the autumn (September) at an altitude of about 98.0 km, with a density of 52.0 cm^{-3}, which corresponds to the sporadic Ca layer.

3.2. Seasonal Variations in Ca and Ca^+ Layer Parameters

For further investigation into the seasonal variations in the Ca and Ca^+ layers, the layer abundances, peak density, centroid altitudes, and RMS widths were extracted from the density depicted in Figure 4. These extracted values were then fitted to a harmonic model described by Equation (2). Figure 5 presents the results for the Ca layer, while Figure 6 displays the corresponding outcomes for the Ca^+ layer.

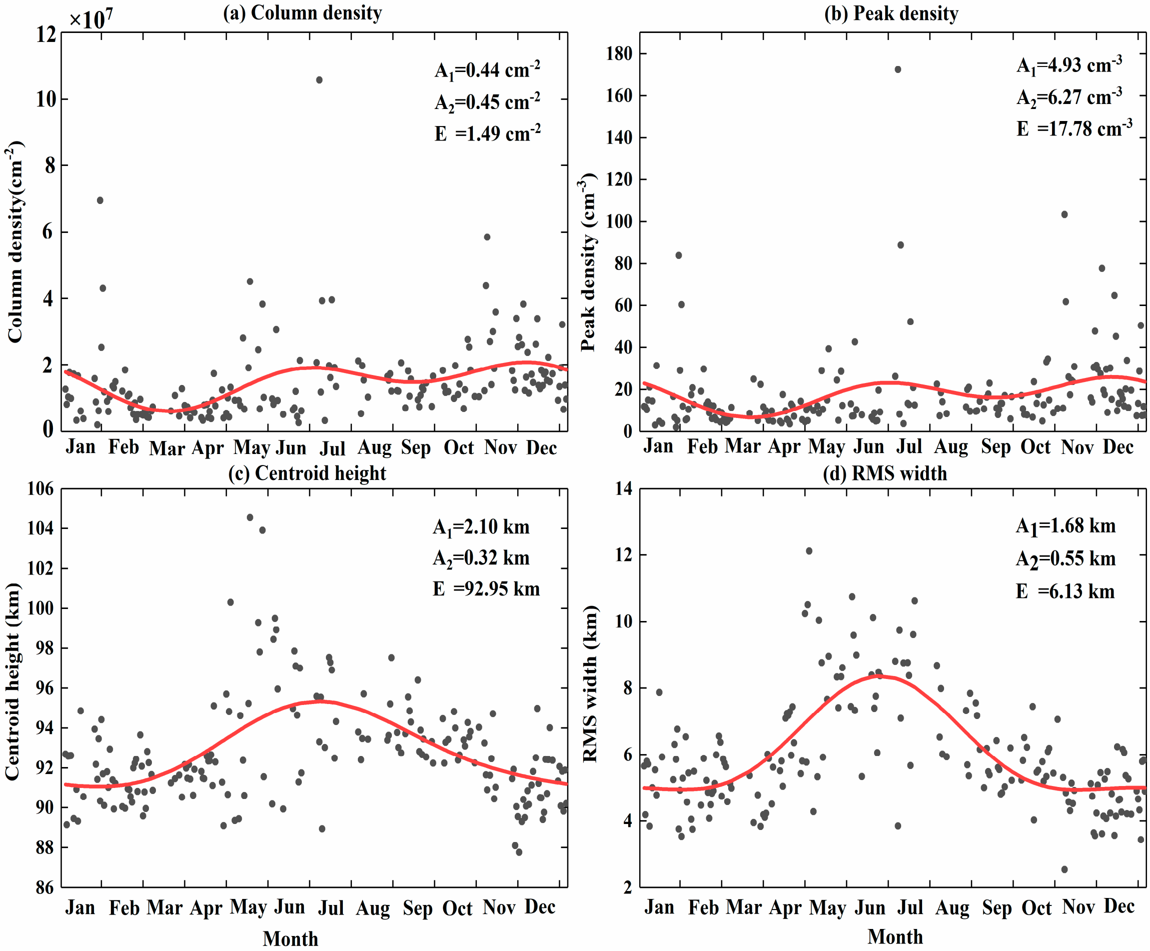

Figure 5. Characterization of the nightly averaged parameters of the calcium atomic layer in Beijing. The red curves are fitted values of the data, and the scattered points are observations of the calcium atomic layer: (**a**) column density, (**b**) peak density, (**c**) centroid height, and (**d**) RMS width.

The annual variation in the column density of the Ca layer, influenced by both annual and semi-annual variations, is depicted in Figure 5a. The annual average column density of the Ca layer is 1.5×10^7 cm^{-2}, with a peak column density of 1.1×10^8 cm^{-2}. There exist two peak values observed in summer (June/July) and early winter (November/December) and two minimum values occurring in spring (March) and autumn (September).

The data presented in Figure 5b illustrate the annual variation in the peak density of the Ca layer. It is evident that the semi-annual harmonics play a significant role in determining the peak density of the Ca layer. Furthermore, the amplitude of the semiannual harmonics is approximately 1.3 times greater than that of the annual harmonics. The Ca layer exhibits an average peak density of around 17.8 cm^{-3}. Notably, this peak density demonstrates two distinct maxima, with values of approximately 23.1 cm^{-3} and 25.8 cm^{-3} occurring in July and December, respectively, and two minimum values are found in March and September. The centroid height of the Ca layer varies between 91.1 km and 95.3 km, with an average centroid height of about 93.0 km and a maximum in June/July. During the summer, the centroid height attains its highest value due to the impact of the sporadic layer.

Figure 4d shows the variation in the RMS width of the Ca layer, exhibiting a resemblance to the seasonal variation in the centroid height. On average, the RMS width of the Ca layer measures approximately 6.1 km.

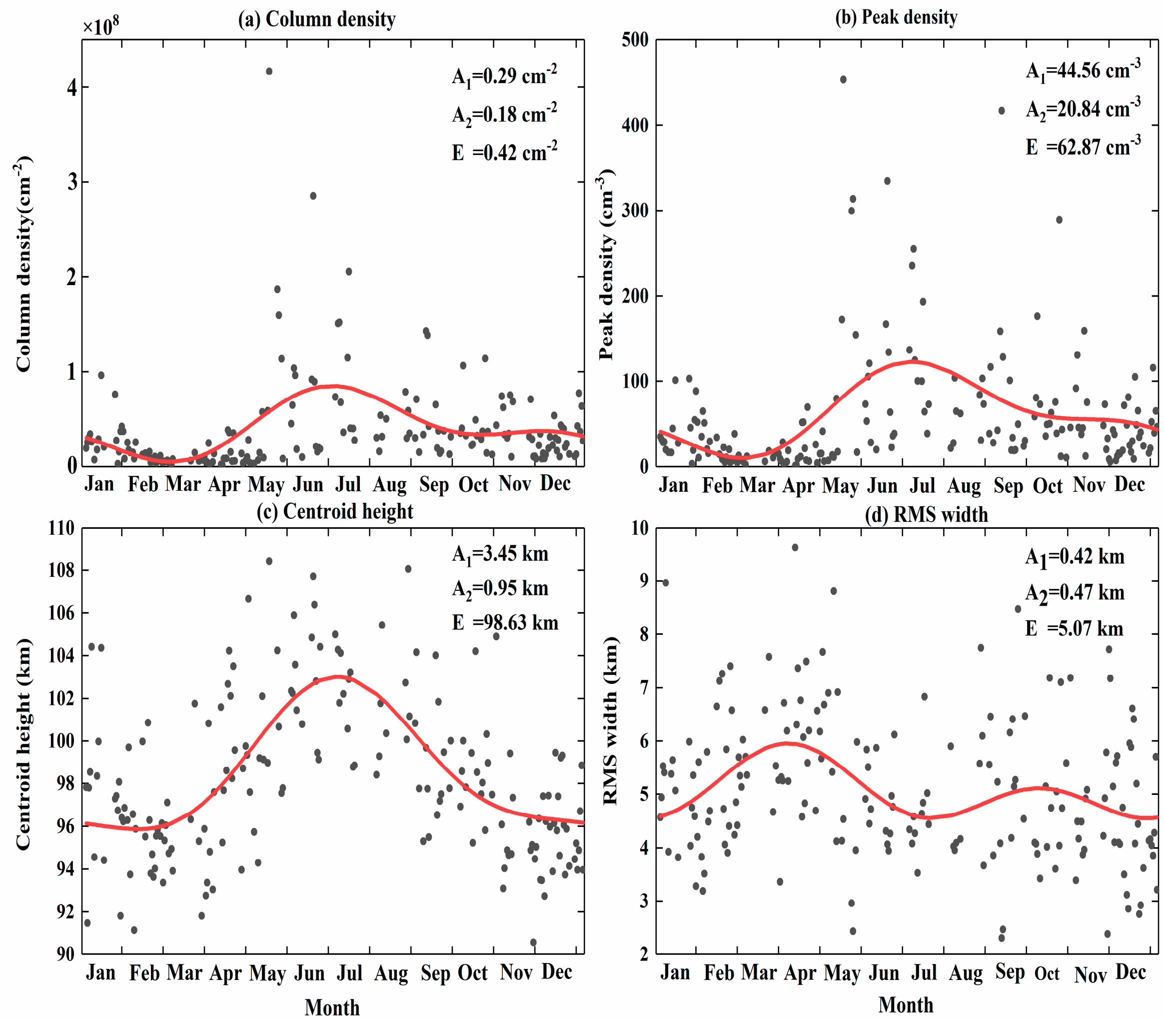

Figure 6. Characterization of the nightly averaged parameters of the calcium ion layer in Beijing. The red curves are fitted values of the data, and the scattered points are observations of the calcium ion layer: (**a**) column density, (**b**) peak density, (**c**) centroid height, and (**d**) RMS width.

Figure 6a displays the column density of the Ca^+ layer, exhibiting a prominent annual variation with an average value of 4.2×10^7 cm^{-2} every year. This value ranged from 1.6×10^6 cm^{-2} to 4.2×10^8 cm^{-2}. The maximum is reached in the summer months (June/July) and the minimum occurs in March. In comparison to the column density of the Ca layer, both exhibit their peak values throughout the summer season. However, it is noteworthy that an additional peak column density of the Ca layer is observed during the winter season. The annual variation in the Ca^+ layer peak density, as depicted in Figure 6b, matches the annual variation observed in the Ca^+ layer column density, with a minimum in spring and maxima in summer. The average peak density is 62.9 cm^{-3}.

Figure 6c illustrates the range of centroid heights observed in the Ca^+ layer from 95.8 km to 103.0 km, with an average centroid height of 98.6 km. The annual variation in the centroid height of the Ca^+ layer is similar to that of the Ca layer. On average, the centroid height of the Ca^+ layer has an elevation approximately 5.6 km greater than that of the Ca layer.

The semiannual variation in the RMS width of the Ca^+ layer is depicted in Figure 6d, exhibiting an annual average of around 5.1 km. There are two maximum values of the Ca^+

layer RMS width occurring in March/April and September/October and a minimum value in July. It is the opposite of the Ca layer RMS width variation.

4. Discussion

4.1. Comparison with Observations at Kühlungsborn (54°N)

The seasonal variation in the Ca layer over Beijing (40.41°N, 116.01°E) is similar to that observed at Kühlungsborn (54°N, 12°E) [9]. This similarity is characterized by three peaks occurring in both winter and summer, while lower densities are observed throughout spring and fall. In summer, the Ca density exhibited its highest levels at both stations, but there are two maxima in Beijing in July. There exists a notable discrepancy between the two winter maxima in Beijing, which transpire in the months of November and February, and those in Kühlungsborn, which transpire in October and January, with the former occurring one month later than the latter. The peak density of the calcium layer above Beijing is approximately half of that observed at Kühlungsborn. The average column density of the calcium layer in Beijing is approximately 71% of that observed in Kühlungsborn. Differences in density may be related to latitude. Recently, we also reported preliminary observations of calcium atoms at Mohe Station (53°N, 122°E) from the 12th of January to the 14th of January, while Kühlungsborn and our team's Mohe Station are at similar latitudes. The maximum Ca density is reported as 53.64 cm^{-3} at the Mohe station in January. The Ca peak densities in Kühlungsborn and Mohe during January exhibit similarities [25].

The densities of the Na layers increase with an increasing latitude [11]. However, the relationship between the latitude and the density of the Ca layer requires additional investigation, particularly with the inclusion of more extensive and prolonged observational data. Furthermore, it was observed that the Beijing Ca layer exhibited TISCa levels ranging from 100 to 115 km from May to August. Referring to Figure 2 in Gerding et al. [9], this particular characteristic was not observed in the seasonal variations in the Kühlungsborn Ca layer. The seasonal variation in the Ca^+ layer in Beijing exhibits similarities to that observed in Kühlungsborn. The density of each of these two exhibits higher values during the months of July (about 102 km) and September (approximately 90 km).

After the meteor is injected into the upper atmosphere, it is affected by chemical and kinetic processes, forming metal atoms and ion layers. The seasonal behavior of the Ca layer at mid-latitudes was simulated and examined by Plane et al. [10]. Their findings revealed a correlation between the seasonal behavior of the Ca density and the meteor input function (Ca MIF). Specifically, the Ca MIF demonstrated a minimum value during the spring season and a maximum value during the autumn season [10]. Referring to Figure 8 in Gerding et al. [9], it is observed that the meteor injection rate is highest in November [9].

Nevertheless, the seasonal variation in the calcium atomic layer during the summer, when it reaches its peak, exhibits significant divergence from that of other metallic elements. There are two primary potential explanations for this phenomenon. One aspect to consider is the differential ablation of meteoritic dust. When meteors penetrate the Earth's atmosphere, distinct components are liberated from the meteors at varying altitudes. This is because their ablation efficiencies are also different. The Na and K exhibit a higher volatility and greater ease of vaporization, while Ca demonstrates a comparatively higher resistance to ablation. So, Ca is less likely to be released from the meteors and remain in the meteor [26,27]. This residual meteoroid creates a photo-sputtering phenomenon that releases calcium atoms from the residual meteoroid. It is worth noting that during the summer, when there are longer daylight hours, the photo-sputtering process becomes more prominent, resulting in an increased production of calcium atoms [9].

Another factor is associated with the neutral chemistry of calcium atoms. The CaO reacts with O_2 and H_2O to produce CaO_3 and $Ca(OH)_2$. The rate of these reactions increases as the temperature decreases. During the summer, the MLT region experiences lower temperatures, as depicted in Figure S1 of the Supplementary Materials. So, these two reactions exhibit increased rates throughout the summer. Also, the H_2O concentration doubles between 80 and 90 km in summer [28]. So, $Ca(OH)_2$ is produced more easily in the summer, and then $Ca(OH)_2$ reacts rapidly with H before Ca is produced via Equation (6), so an extremely large maximum occurs in the summer [9,10].

$$\mathrm{CaO + O_2(+M) \rightarrow CaO_3} \tag{3}$$

$$\mathrm{CaO + H_2O(+M) \rightarrow Ca(OH)_2} \tag{4}$$

$$\mathrm{Ca(OH)_2 + H \rightarrow CaOH + H_2O} \tag{5}$$

$$\mathrm{CaOH + H \rightarrow Ca + H_2O} \tag{6}$$

The occurrence of Ca^+s is observed at a near-daily frequency. Consequently, there is a notable disparity between the seasonal variations observed in Ca^+ layers and those observed in Ca layers. The Ca^+ layer exhibits its highest density from May to July, reaching its maximum altitude at around 105 km, which corresponds to the appearance of TISCa from May to July. It corresponds to the frequent occurrence of Es in summer [29].

We observed that the centroid altitude in our study is higher than the earlier observations from Kühlungsborn (1996–1998). This difference can be attributed to two main factors. First, during the months of May to August, there is a frequent occurrence of sporadic Ca layers in the altitude range of 95–115 km at Yanqing, contributing to an elevation in the average centroid altitude. Second, except for the period of May to August, the centroid altitude of calcium atoms at Yanqing is slightly higher (less than 1 km) than that observed in Kühlungsborn. It is noteworthy that She et al., 2023, reported a declining trend in the centroid altitude of sodium atoms from 1990 to 2017, correlating with solar flux [30]. To further explore this, we calculated the monthly average sunspot number, obtaining a mean of 56.69/month for December 1996 to December 1998 and 34.13/month for March 2020 to July 2022. The higher observed centroid altitude in our study may be related to the weaker solar activity during the selected time period.

4.2. Comparison with the Observation of Na, Ni, and K at the Same Station

Furthermore, alongside the concurrent observations of Ca and Ca^+, the observation of Na, Ni, and K has also been observed at Yanqing station. The seasonal variations in this were reported in 2017 and 2022, respectively [17,31]. We compared the seasonal variations of the four atoms and found that the Ca layer displays semiannual variations, with a maximum density in summer and winter and a minimum density in spring and autumn. In comparison, the Na layer in Beijing displays significant annual variations, wherein the highest peak density is observed in January (~4000 cm^{-3}) at an altitude of around 91 km. This peak density is found to be 173 times greater than the peak density of the Ca layer, as shown by the Na layer density reference [31] and illustrated in Figure 4a. The density of the Ni layer exhibits comparable variations to that of the Na layer, characterized by a decrease during the summer and an increase during the winter. The Ni peak density is around 400 cm^{-3}, which is 17 times more than the peak density of the Ca layer. This information can be found in the reference [31] and is illustrated in Figure 3a. The K layer in Beijing exhibits a distinct semiannual variation, characterized by peak values during the winter and summer and trough values during the spring and autumn. Specifically, the highest density is observed in winter (January), reaching approximately 110 cm^{-3}, which is five times greater than the maximum density observed in the Ca layer (reference [17], Figure 7).

The average column densities of the Na, Ni, and K layers were 2. 5×10^9 cm^{-2}, 3.1×10^8 cm^{-2}, and 8.41×10^7 cm^{-2}. They are about 167, 21 and 6 times that of Ca. The maximum column densities of the Na, Ni, and K layers were about 5.8×10^9 cm^{-2}, 5.7×10^8 cm^{-2}, and 2.51×10^8 cm^{-2}, and they are about 52.7, 5.2, and 2.3 times that of Ca. It may be related to the abundance of elements in meteorite particles and the ablation efficiency of meteors. For example, the ablation efficiency of Ca is an order of magnitude lower than that of Na [32]. The Ca has a higher abundance in meteorite particles (CI) than K [33], but the K is more volatile than metallic Ca and is more easily ablated into the atmosphere [27].

In Figure 4a, a thermosphere–ionosphere sporadic calcium layer (TISCa) occurs between 100 and 115 km from May to August, which is also observed in the TISNi layer (~110 km) in summer. However, from the seasonal variations in Na and K layers in Beijing, the TISNa and TISK were unnoticeable. In addition, we observed a maximum of Na, K, and Ca layers in the summer, but the Ni layer only had a maximum in winter [17,31].

There exist two primary methods for the generation of metal atoms in general. There are two distinct processes involved in the reaction of ionic compounds: dissociative recombination and the direct neutralization of metal ions through electron transfer. Wu et al. [34] reported on the TISNi and TISNa layers seen in Beijing, spanning from 105 km to 120 km. Their findings indicate that TISNi and TISNa have similar formation mechanisms.

They mainly originate from the direct neutralization of Ni^+ and Na^+ with electrons [34]. To explore the formation of TISCa at 100 km to 115 km, this paper uses the ion–molecule reactions in Plane et al. [3] and Plane et al. [10] to deduce the first-order neutralization rates of Ca^+ [35–37] (see the Supplementary Materials), and the first-order neutralization rates of Na^+, Ni^+, and K^+ are derived from Jiao et al. [35] and Wu et al. [34]. Finally, the first-order neutralization rate curves for the dissociative recombination and direct recombination of metal Na^+, Ni^+, K^+, and Ca^+ at f_0Es = 10 MHz are plotted in Figure 7. Above 105 km, Na^+, Ni^+, and Ca^+ are mainly dominated by direct recombination. The direct recombination rate of Ni^+ is an order of magnitude larger than that of Na^+ and Ca^+. Although the direct recombination rates of Na^+ and Ca^+ are similar, the dissociative recombination rate of Ca^+ is 2–10 times greater than that of Na^+. Another important reason is that the density of the main Ca layer is one to two orders of magnitude lower than that of the Na layer. So, the density ratio of TISCa to the main layer is higher, and it is more obvious in seasonal variations above 100 km. The dissociative recombination rate of K^+ is the slowest of the four metals, and therefore, TISK is not obvious in the seasonal variation.

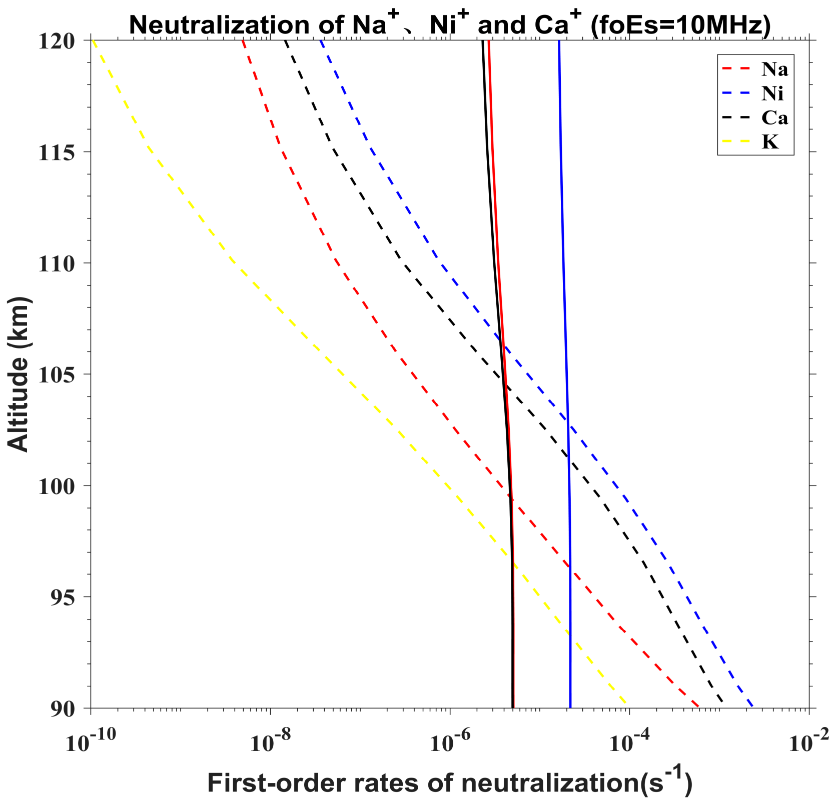

Figure 7. First-order neutralization rates for the dissociative recombination (dashed line) and direct recombination (solid line) of Na^+(red), Ni^+(bule), Ca^+(black), and K^+(yellow).

5. Conclusions

This study presents the collection of data on calcium atoms and calcium ions for a period exceeding two years. The data were obtained through the utilization of an all-solid-state, dual-wavelength, narrow-band lidar system. This is the first time seasonal analyses are presented in the mid-latitude of Asia (Beijing (40.41°N, 116.01°E)).

The layers of Ca and Ca^+ observed at a latitude of 40.41°N exhibit the following annual mean characteristics: The Ca column density ranges from 2.0×10^6 to 1.1×10^8 atoms cm^{-2}, with an average centroid height of 93.0 km. Regarding Ca^+, the column density varies from 1.6×10^6 to 4.2×10^8 atoms cm^{-2}, with an average centroid height of 98.6 km. The column density of the Ca^+ layer shows a general annual variation with a minimum in March and a maximum almost from in June/July, while the Ca column density is a combination of annual and semiannual oscillations with maximum around late November/December.

The seasonal variations in the Ca layer are mainly in the range of 80.6~103.7 km, which is comparable to the distribution range of seasonal variations observed in the Na, K, and Ni layers in Beijing. The seasonal variation in the Ca^+ layer is mainly reflected in 100~115 km, and the Ca^+ layer corresponds to the Ca layer in 95~116 km.

However, it should be noted that the Ca layer and Ca^+ layer do not exhibit a direct correspondence with each other within the altitude range of 80~95 km. In our further research, we intend to provide additional analyses on the underlying Ca layer and the background Ca^+ layer while excluding the sporadic Ca layer and sporadic Ca^+ layer.

The seasonal variations in the Ca and Ca^+ layers in Beijing (40.41°N) are similar to those reported in Kühlungsborn (54°N), and the peak densities of Ca^+ layers are similar too. The significant difference is that the peak density of Ca layers in Beijing is half that of Ca layers in Kühlungsborn. This discrepancy in density could potentially be attributed to the geographical latitude of the respective locations.

Compared with the seasonal variations in Na, Ni, and K at the same station, their average column abundances are approximately 167, 21, and 6 times more than those of calcium atoms, respectively, and from May to July, the Ca layer has an apparent three-layer structure. These phenomena could perhaps be attributed to the selective removal of various components during the process of meteoric injection, as well as notable variations in ion–molecule reactions.

Supplementary Materials: The following supporting information can be downloaded at: https://www.mdpi.com/article/10.3390/rs16030596/s1, Figure S1: Annual variation in the 80~100 km mean temperature over Beijing with time (temperature data from WACCM); Table S1: Ca Ion–Molecule Reactions and Rate Coefficients. This supplementary material also contains a first-order neutralization rate derivation for Ca^+.

Author Contributions: Conceptualization, G.Y. and Y.X.; methodology, Y.X., G.Y. and Z.W.; software, P.Z., Y.X., Z.W. and Z.C.; validation, Y.X., G.Y. and Z.W.; formal analysis, P.Z.; investigation, Y.X. and P.Z.; resources, G.Y. and Y.X.; data curation, L.D. and H.Z.; writing—original draft preparation, Y.X. and P.Z.; writing—review and editing, G.Y., L.D., J.J., S.G., Z.W. and Z.C.; visualization, P.Z.; supervision, G.Y.; project administration, H.Z.; funding acquisition, G.Y and Y.X. All authors have read and agreed to the published version of the manuscript.

Funding: This research was supported by the National Natural Science Foundation of China (42004134, 42374204, 41627804), Specialized Research Fund for State Key Laboratories (Y32612A24S), State Key Laboratory of Space Weather, Chinese Meridian Project, International Partnership Program of Chinese Academy of Sciences (183311KYSB20200003), Scientific Projects of Hainan Province (ZDYF2021GXJS040), the Innovational Fund for Scientific and Technological Personnel of Hainan Province (KJRC2023C05) and Chinese Academy of Sciences (YSBR-018).

Data Availability Statement: Data is available online https://data.mendeley.com/datasets/ (accessed on 9 November 2023).

Acknowledgments: The authors are grateful to the Chinese Meridian Project for providing the equipment and data. The authors thank all anonymous reviewers and editors for their constructive review of this manuscript.

Conflicts of Interest: The authors declare no conflicts of interest.

References

1. Xun, Y.; Yang, G.; She, C.Y.; Wang, J.; Du, L.; Yan, Z.; Yang, Y.; Cheng, X.; Li, F. The first concurrent observations of thermospheric Na layers from two nearby central midlatitude lidar stations. *Geophys. Res. Lett.* **2019**, *46*, 1892–1899. [CrossRef]
2. Jiao, J.; Chu, X.; Jin, H.; Wang, Z.; Xun, Y.; Du, L.; Zheng, H.; Wu, F.; Xu, J.; Yuan, W.; et al. First lidar profiling of meteoric Ca^+ ion transport from ~80 to 300 km in the midlatitude nighttime ionosphere. *Geophys. Res. Lett.* **2022**, *49*, e2022GL100537. [CrossRef]
3. Plane, J.M.; Feng, W.; Dawkins, E.C. The mesosphere and metals: Chemistry and changes. *Chem. Rev.* **2015**, *115*, 4497–4541. [CrossRef] [PubMed]
4. Slipher, V. Emission in the spectrum of the light of the night sky. *Publ. Astron. Soc. Pac.* **1929**, *41*, 262–263.
5. Alpers, M.; Höfffner, J.; von Zahn, U. Upper atmosphere Ca and Ca^+ at mid-latitudes: First simultaneous and common-volume lidar observations. *Geophys. Res. Lett.* **1996**, *23*, 567–570. [CrossRef]
6. Granier, G.; Jégou, J.-P.; Mégie, G. Resonant lidar detection of Ca and Ca^+ in the upper atmosphere. *Geophys. Res. Lett.* **1985**, *12*, 655–658. [CrossRef]
7. Granier, C.; Jegou, J.; Megie, G. Atomic and ionic calcium in the Earth's upper atmosphere. *J. Geophys. Res. Atmos.* **1989**, *94*, 9917–9924. [CrossRef]
8. Qian, J.; Gardner, C.S. Simultaneous lidar measurements of mesospheric Ca, Na, and temperature profiles at Urbana, Illinois. *J. Geophys. Res. Atmos.* **1995**, *100*, 7453–7461. [CrossRef]
9. Gerding, M.; Alpers, M.; von Zahn, U.; Rollason, R.J.; Plane, J.M.C. Atmospheric Ca and Ca^+ layers: Midlatitude observations and modeling. *J. Geophys. Res. Space Phys.* **2000**, *105*, 27131–27146. [CrossRef]
10. Plane, J.; Feng, W.; Gómez Martín, J.C.; Gerding, M.; Raizada, S. A new model of meteoric calcium in the mesosphere and lower thermosphere. *Atmos. Chem. Phys.* **2018**, *18*, 14799–14811. [CrossRef]
11. Gong, S.; Yang, G.; Xu, J.; Xue, X.; Jiao, J.; Tian, D.; Fu, J.; Liu, Z. Lidar studies on the nighttime and seasonal variations of background sodium layer at different latitudes in China. *Chin. J. Geophys.* **2013**, *56*, 2511–2521. (In Chinese) [CrossRef]
12. Yi, F.; Yu, C.; Zhang, S.; Yue, X.; He, Y.; Huang, C.; Zhang, Y.; Huang, K. Seasonal variations of the nocturnal mesospheric Na and Fe layers at 30°N. *J. Geophys. Res. Atmos.* **2009**, *114*. [CrossRef]
13. Gardner, C.S.; Plane, J.M.; Pan, W.; Vondrak, T.; Murray, B.J.; Chu, X. Seasonal variations of the Na and Fe layers at the South Pole and their implications for the chemistry and general circulation of the polar mesosphere. *J. Geophys. Res. Atmos.* **2005**, *110*. [CrossRef]
14. Raizada, S.; Tepley, C.A. Seasonal variation of mesospheric iron layers at Arecibo: First results from low-latitudes. *Geophys. Res. Lett.* **2003**, *30*. [CrossRef]
15. Eska, V.; Höffner, J.; Von Zahn, U. Upper atmosphere potassium layer and its seasonal variations at 54°N. *J. Geophys. Res. Space Phys.* **1998**, *103*, 29207–29214. [CrossRef]
16. Yue, X.; Friedman, J.S.; Wu, X.; Zhou, Q.H. Structure and seasonal variations of the nocturnal mesospheric K layer at Arecibo. *J. Geophys. Res. Atmos.* **2017**, *122*, 7260–7275. [CrossRef]
17. Wang, Z.; Yang, G.; Wang, J.; Yue, C.; Yang, Y.; Jiao, J.; Du, L.; Cheng, X.; Chi, W. Seasonal variations of meteoric potassium layer over Beijing (40.41° N, 116.01° E). *J. Geophys. Res. Space Phys.* **2017**, *122*, 2106–2118. [CrossRef]
18. Mahnke, P.; Klingenberg, H.H.; Fix, A.; Wirth, M. Dependency of injection seeding and spectral purity of a single resonant KTP optical parametric oscillator on the phase matching condition. *Appl. Phys. B* **2007**, *89*, 1–7. [CrossRef]
19. Velarde, L.; Engelhart, D.P.; Matsiev, D.; LaRue, J.; Auerbach, D.J.; Wodtke, A.M. Generation of tunable narrow bandwidth nanosecond pulses in the deep ultraviolet for efficient optical pumping and high resolution spectroscopy. *Rev. Sci. Instrum.* **2010**, *81*, 063106. [CrossRef]
20. Du, L.; Zheng, H.; Xiao, C.; Cheng, X.; Wu, F.; Jiao, J.; Xun, Y.; Chen, Z.; Wang, J.; Yang, G. The All-Solid-State Narrowband Lidar Developed by Optical Parametric Oscillator/Amplifier (OPO/OPA) Technology for Simultaneous Detection of the Ca and Ca^+ Layers. *Remote Sens.* **2023**, *15*, 4566. [CrossRef]
21. Gardner, C.S.; Chu, X.; Espy, P.J.; Plane, J.M.; Marsh, D.R.; Janches, D. Seasonal variations of the mesospheric Fe layer at Rothera, Antarctica (67.5° S, 68.0° W). *J. Geophys. Res. Atmos.* **2011**, *116*. [CrossRef]
22. Gardner, C.; Voelz, D.; Sechrist, C., Jr.; Segal, A. Lidar studies of the nighttime sodium layer over Urbana, Illinois: 1. Seasonal and nocturnal variations. *J. Geophys. Res. Space Phys.* **1986**, *91*, 13659–13673. [CrossRef]
23. Gerding, M.; Alpers, M.; Höffner, J.; Zahn, U.V. Sporadic Ca and Ca^+ layers at mid-latitudes: Simultaneous observations and implications for their formation. *Ann. Geophys.* **2003**, *19*, 47–58. [CrossRef]
24. Dou, X.K.; Qiu, S.C.; Xue, X.H.; Chen, T.D.; Ning, B.Q. Sporadic and thermospheric enhanced sodium layers observed by a lidar chain over China. *J. Geophys. Res. Space Phys.* **2013**, *118*, 6627–6643. [CrossRef]
25. Chen, F.; Xun, Y.; Wang, Z.; Du, L.; Zheng, H.; Chen, Z.; Cheng, X.; Wang, J.; Wu, F.; Yang, G. Preliminary results of Calcium atom analysis by the wind-temperature-metal-constituents LiDAR at Mohe middle upper atmosphere, for the Chinese Meridian Project Phase II. *Rev. Geophys. Planet. Phys.* **2023**, *54*, 1–7. (In Chinese) [CrossRef]
26. McNeil, W.J.; Lai, S.T.; Murad, E. Models of thermospheric sodium, calcium and magnesium at the magnetic equator. *Adv. Space Res.* **1998**, *21*, 863–866. [CrossRef]

27. Von Zahn, U.; Gerding, M.; Höffner, J.; McNeil, W.; Murad, E. Iron, calcium, and potassium atom densities in the trails of Leonids and other meteors: Strong evidence for differential ablation. *Meteorit. Planet. Sci.* **1999**, *34*, 1017–1027. [CrossRef]
28. Plane, J.M.; Gardner, C.S.; Yu, J.; She, C.; Garcia, R.R.; Pumphrey, H.C. Mesospheric Na layer at 40° N: Modeling and observations. *J. Geophys. Res. Atmos.* **1999**, *104*, 3773–3788. [CrossRef]
29. Raizada, S.; Tepley, C.A.; Williams, B.P.; García, R. Summer to winter variability in mesospheric calcium ion distribution and its dependence on Sporadic E at Arecibo. *J. Geophys. Res. Space Phys.* **2012**, *117*. [CrossRef]
30. She, C.Y.; Krueger, D.A.; Yan, Z.A.; Yuan, T.; Smith, A.K. Climatology, Long-Term Trend and Solar Response of Na Density Based on 28 Years (1990–2017) of Midlatitude Mesopause Na Lidar Observation. *J. Geophys. Res. Space Phys.* **2023**, *128*. [CrossRef]
31. Jiao, J.; Feng, W.; Wu, F.; Wu, F.; Zheng, H.; Du, L.; Yang, G.; Plane, J. A Comparison of the midlatitude nickel and sodium layers in the mesosphere: Observations and modeling. *J. Geophys. Res. Space Phys.* **2022**, *127*, e2021JA030170. [CrossRef]
32. Carrillo-Sánchez, J.; Nesvorný, D.; Pokorný, P.; Janches, D.; Plane, J. Sources of cosmic dust in the Earth's atmosphere. *Geophys. Res. Lett.* **2016**, *43*, 11979–11986. [CrossRef] [PubMed]
33. Asplund, M.; Grevesse, N.; Sauval, A.J.; Scott, P. The chemical composition of the Sun. *Annu. Rev. Astron. Astrophys.* **2009**, *47*, 481–522. [CrossRef]
34. Wu, F.; Chu, X.; Du, L.; Jiao, J.; Zheng, H.; Xun, Y.; Feng, W.; Plane, J.M.; Yang, G. First Simultaneous Lidar Observations of Thermosphere-Ionosphere Sporadic Ni and Na (TISNi and TISNa) Layers (~105–120 km) Over Beijing (40.42° N, 116.02° E). *Geophys. Res. Lett.* **2022**, *49*, e2022GL100397. [CrossRef]
35. Jiao, J.; Yang, G.; Wang, J.; Feng, W.; Plane, J. Observations of dramatic enhancements to the mesospheric K layer. *Geophys. Res. Lett.* **2017**, *44*, 12536–12542. [CrossRef]
36. Qiu, S.; Wang, N.; Soon, W.; Lu, G.; Jia, M.; Wang, X.; Xue, X.; Li, T.; Dou, X. The sporadic sodium layer: A possible tracer for the conjunction between the upper and lower atmospheres. *Atmos. Chem. Phys.* **2021**, *21*, 11927–11940. [CrossRef]
37. Plane, J. A new time-resolved model of the mesospheric Na layer: Constraints on the meteor input function. *Atmos. Chem. Phys. Discuss.* **2004**, *4*, 39–69.